




 Cite this: *RSC Adv.*, 2021, 11, 40235

 Received 23rd October 2021  
 Accepted 8th December 2021

DOI: 10.1039/d1ra07841k

rsc.li/rsc-advances

# Molecule-like cluster magnetism and cationic order in the new hexagonal perovskite $\text{Ba}_4\text{Sn}_{1.1}\text{Mn}_{2.9}\text{O}_{12}$ †

 Junkun Wu,<sup>a</sup> Xiaohui Yan,<sup>a</sup> Wenbin Guo,<sup>a</sup> Xiaoming Wang,<sup>b</sup> Congling Yin <sup>\*a</sup> and Xiaojun Kuang <sup>\*ac</sup>

The new hexagonal perovskite phase of composition  $\text{Ba}_4\text{Sn}_{1.1}\text{Mn}_{2.9}\text{O}_{12}$  has been synthesized by solid-state reactions at 1673 K. The crystal structure has been investigated using X-ray and neutron diffraction. The hexagonal perovskite structure has an ordered arrangement of Sn and Mn ions on the corner-sharing octahedral centers and the face-sharing octahedral centers respectively. Short Mn–Mn distances have been evidenced in the face-sharing trimer of  $\text{MnO}_6$  octahedra. The magnetic susceptibility shows magnetic cluster behavior, with cluster formation temperature  $\sim 220$  K. Antiferromagnetic order has been observed at  $T_N \sim 6$  K.  $\text{Ba}_4\text{Sn}_{1.1}\text{Mn}_{2.9}\text{O}_{12}$  is a semiconductor with a transport activation energy of 0.61 eV.

## 1 Introduction

Manganese oxides have attracted enormous attention during the last decades mainly due to their technological applications as heterogeneous catalysts,<sup>1</sup> Li batteries,<sup>2,3</sup> SOFC electrode materials,<sup>4</sup> and magnetic<sup>5</sup> and also CMR materials.<sup>6</sup> This has motivated the investigation of the hexagonal perovskite  $\text{BaMnO}_{3-\delta}$  system, which shows a diversity of crystal structures and magnetic properties.<sup>7–11</sup> A series of  $\text{BaMnO}_{3-\delta}$  polytypes have been found, for example,  $2\text{H} \rightarrow 15\text{R} \rightarrow 8\text{H} \rightarrow 6\text{H} \rightarrow 10\text{H} \rightarrow 4\text{H}$ , as the oxygen vacancy  $\delta$  increases.<sup>7,10</sup> Additional polymorphs (*i.e.*  $9\text{R}-\text{Ba}_{0.875}\text{Sr}_{0.125}\text{MnO}_3$ ) are generated upon Sr substitution on the Ba site.<sup>10</sup> Further perovskite polytypes may be produced when Mn is replaced by other cations.

Many Mn-substituted  $\text{BaM}_x\text{Mn}_{1-x}\text{O}_3$  systems have been investigated, for instance, with  $\text{M} = \text{Ca}$ ,<sup>12,13</sup>  $\text{Ti}$ ,<sup>14,15</sup>  $\text{In}$ ,<sup>16,17</sup>  $\text{Sn}$ ,<sup>18</sup>  $\text{Sb}$ ,<sup>19</sup>  $\text{Fe}$ ,<sup>20</sup>  $\text{Ru}$ ,<sup>21,22</sup>  $\text{Ir}$ ,<sup>23</sup> and rare earth Ln.<sup>24,25</sup> This led to the uncovering of a range of M-cation (partially) ordered 12R perovskites  $\text{Ba}_4\text{Ti}_2\text{Mn}_2\text{O}_{12}$ ,<sup>14</sup>  $\text{Ba}_4\text{InMn}_3\text{O}_{11.5}$ ,<sup>16</sup>  $\text{Ba}_4\text{RE}\text{Mn}_3\text{O}_{12}$  ( $\text{RE} = \text{Ce}$  and  $\text{Pr}$ ),<sup>24</sup>  $\text{Ba}_4\text{YMn}_3\text{O}_{11.5}$ ,<sup>26</sup> and  $\text{Ba}_4\text{NbMn}_3\text{O}_{12}$ .<sup>27</sup> The  $\text{Ba}_4\text{MMn}_3\text{O}_{12}$  12R perovskite consists of close-packed  $\text{BaO}_3$  layers in a (cchh)<sub>3</sub> sequence. The larger-sized substituted M ions are hosted in the corner-sharing octahedral center M1, and the

Mn ions occupy the face-sharing octahedral centers M2 and M3, as shown in Fig. 1a. Partial disorder of M and Mn elements occurs on the M2 site when the M ion has a similar size with 6-coordinated  $\text{Mn}^{4+}$  (0.53 Å), *i.e.*  $\text{Ti}^{4+}$  (0.605 Å, CN = 6).<sup>28</sup>

The  $\text{BaMnO}_{3-\delta}$  polymorphs show the long-range antiferromagnetic (AFM) order of all the Mn spins, with  $T_N = 220\text{--}270$  K.<sup>9,10</sup> However, the magnetic order is suppressed in the 12R perovskites with trimers of face-sharing  $\text{MnO}_6$  octahedra on low-content nonmagnetic doping. No magnetic order is observed for  $\text{Ba}_4\text{InMn}_3\text{O}_{11.5}$  (ref. 16) and  $\text{Ba}_4\text{Ti}_2\text{Mn}_2\text{O}_{12}$ ,<sup>14</sup> whilst  $\text{Ba}_4\text{YMn}_3\text{O}_{11.5}$  (ref. 26) and  $\text{Ba}_4\text{CeMn}_3\text{O}_{12}$  (ref. 29) undergoes an AFM transition at  $T_N = 4\text{--}6$  K. The  $\text{Ba}_4\text{NbMn}_3\text{O}_{12}$  sample experiences a ferrimagnetic transition at 42 K and an additional

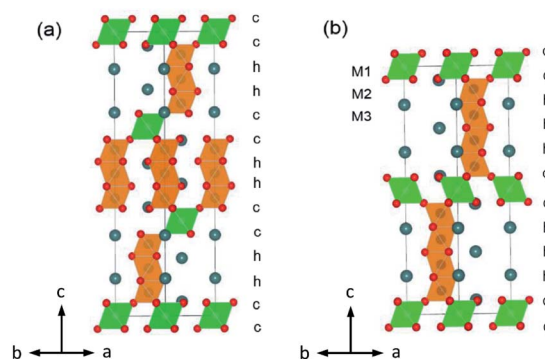


**Fig. 1** The crystal structures viewed along [110] of (a) 12R  $\text{Ba}_4\text{MMn}_3\text{O}_{12}$  and (b) 10H  $\text{Ba}_5\text{MMn}_4\text{O}_{15}$ , showing the stacking sequence of  $\text{BaO}_3$  and corner-sharing octahedron center M1 and face-sharing octahedron center M2 and M3. The  $\text{MnO}_6$  and  $\text{MO}_6$  octahedra are shaded in yellow and green respectively. The barium and oxygen atoms are shown as large cyan and small red spheres.

<sup>a</sup>MOE Key Laboratory of New Processing Technology for Nonferrous Metal and Materials, Guangxi Key Laboratory of Optic and Electronic Materials and Devices, College of Materials Science and Engineering, Guilin University of Technology, Guilin 541004, P. R. China. E-mail: congling.yin@glut.edu.cn

<sup>b</sup>Key Lab Macromolecular Science of Shaanxi Province, College of Chemistry and Chemical Engineering, Shaanxi Normal University, Xian 710062, P. R. China

<sup>c</sup>College of Chemistry and Bioengineering, Guilin University of Technology, Guilin 541004, P. R. China

† CCDC 2117124. For crystallographic data in CIF or other electronic format see DOI: 10.1039/d1ra07841k



magnetic abnormality at  $\sim 6$  K.<sup>27</sup> The latter one should be AFM transition, as suggested by first-principle calculations.<sup>30</sup> Furthermore,  $\text{Ba}_4\text{NbMn}_3\text{O}_{12}$  and  $\text{Ba}_4\text{Ti}_2\text{Mn}_2\text{O}_{12}$  show cluster magnetism, with linear  $\text{Mn}_3$  (and  $\text{Mn}_2$ ) magnetic clusters arranged in triangular plains, leading to magnetic frustrations.<sup>30,31</sup> Therefore, the 12R perovskite materials are potential quantum materials, such as quantum spin liquid.<sup>32,33</sup> The exploration of new 12R perovskite  $\text{BaM}_x\text{Mn}_{1-x}\text{O}_3$  is of great interest.

The  $\text{BaSn}_{1-x}\text{Mn}_x\text{O}_3$  system contains one cation-ordered perovskite 10H  $\text{Ba}_5\text{Sn}_{1.1}\text{Mn}_{3.9}\text{O}_{15}$ .<sup>18</sup> The  $\text{Ba}_5\text{MMn}_4\text{O}_{15}$  10H polype has close-packed  $\text{BaO}_3$  layers in (cchhh)<sub>2</sub> sequences, and features tetramers of face-sharing  $\text{MnO}_6$  octahedra, alternating with  $\text{MO}_6$  octahedra (Fig. 1b). Considering the close relationship between the 10H and 12R perovskites, we wonder whether the 12R polymorph  $\text{BaSn}_{1-x}\text{Mn}_x\text{O}_3$  can exit. If the 12R  $\text{BaSn}_{1-x}\text{Mn}_x\text{O}_3$  is stabilized, it would be a good material with magnetic clusters and frustration. Motivated by such ideas, we investigate a series of  $\text{BaSn}_{1-x}\text{Mn}_x\text{O}_3$ . Herein we report the synthesis, crystal structure, and physical properties of 12R  $\text{Ba}_4\text{Sn}_{1.1}\text{Mn}_{2.9}\text{O}_{12}$  perovskite.

## 2 Experimental

### 2.1 Synthesis

The polycrystalline  $\text{Ba}_4\text{Sn}_{1+x}\text{Mn}_{3-x}\text{O}_{12}$  ( $-0.1 < x < 0.2$ ) were prepared *via* high-temperature solid-state reaction, using  $\text{BaCO}_3$  (99.5%, Alfa Aesar),  $\text{SnO}_2$  (99%, Alfa Aesar), and  $\text{MnO}_2$  (99.5%, Alfa Aesar) reagents as raw materials. These starting materials were carefully weighed according to the correct stoichiometries, and mixed thoroughly with alcohol in an agate mortar and pestle, and heated in an alumina crucible at 1273 K for 10 h to decompose the carbonate. Then the material was reground, pressed into pellets (20 tons per  $\text{cm}^2$ ), and placed on the platinum foil, and sintered at 1673 K for a total of 24 h with heating and cooling rates of  $5 \text{ K min}^{-1}$ , leading to dense pellet ceramic samples. At several intervening steps, the material was re-ground and re-pressed, and powder X-ray diffraction (XRD) was performed at each step to track the reaction to completion. The densities of the final ceramic pellets were calculated using their geometric sizes (diameters and thicknesses) and the masses.

### 2.2 Characterization

The phase purity of the samples was characterized by XRD using a Panalytical X'pert Powder diffractometer with  $\text{Cu K}\alpha$  radiation operated at 40 kV and 40 mA. Data were collected over the  $2\theta$  range  $5\text{--}120^\circ$  for Rietveld analysis carried out using the Topas Academic software.<sup>34</sup> Bond valence sums (BVS) were calculated by Brown and Altermatt's method.<sup>35</sup>

Time-of-flight (TOF) neutron diffraction data were collected from  $\sim 5$  g fine powder samples of  $\text{Ba}_4\text{Sn}_{1.1}\text{Mn}_{2.9}\text{O}_{12}$  using the general-purpose powder diffractometer (GPPD) at the China Spallation Neutron Source (CSNS). Selected area electron diffraction (SAED) patterns were recorded using a JEOL JEM-

2100F transmission electron microscopy (TEM) with a point resolution of  $1.9 \text{ \AA}$  and operated at 200 kV.

Magnetic susceptibility data were acquired using a Quantum Design MPMS-3 superconducting quantum interference device (SQUID) magnetometer. DC magnetic susceptibilities were recorded in a 1000 Oe applied field while warming the sample from 2 to 300 K, following both zero-field cooling (ZFC) and field cooling (FC). AC magnetic susceptibilities from 2 K to 10 K were also measured at step mode at different frequencies of 100 Hz, 250 Hz, 500 Hz, and 1000 Hz.

AC impedance spectroscopy (IS) measurements were carried out from room temperature (RT) to 773 K using a Solartron 1260 frequency response analyzer over the  $10^{-1}\text{--}10^7$  Hz frequency range. Before the IS measurements, the silver paste was coated on the opposite faces of the pellets and fired at 823 K for 30 min to remove the organic component and form electrodes. The impedance data analysis and equivalent circuit fitting were carried out with Zview software.

Inductively coupled plasma optical emission spectroscopy (ICP-OES) was performed on the  $\text{Ba}_4\text{Sn}_{1.1}\text{Mn}_{2.9}\text{O}_{12}$  sample to determine the cationic contents using a PerkinElmer Optima 8000 inductively coupled plasma optical emission spectrometer. The scanning electron microscopy (SEM) imaging and X-ray energy dispersive spectroscopy (EDS) elemental analysis were performed using a GeminiSEM 300 (ZEISS, Germany) scanning electron microscope equipped with an Ultim Max (Oxford, U.K.) EDS spectrometer.

## 3 Results and discussions

### 3.1 Phase formation

The initial  $\text{Ba}_4\text{SnMn}_3\text{O}_{12}$  samples consisted of mixed 12R and 10H perovskite phases (Fig. 2). The Sn doping amount was varied to eliminate the 10H phase, and the XRD patterns of the  $\text{Ba}_4\text{Sn}_{1+x}\text{Mn}_{3-x}\text{O}_{12}$  are shown in Fig. 2. The amount of the 10H phase is reduced at an increase of  $x$  from  $-0.1$  to  $0.1$  and

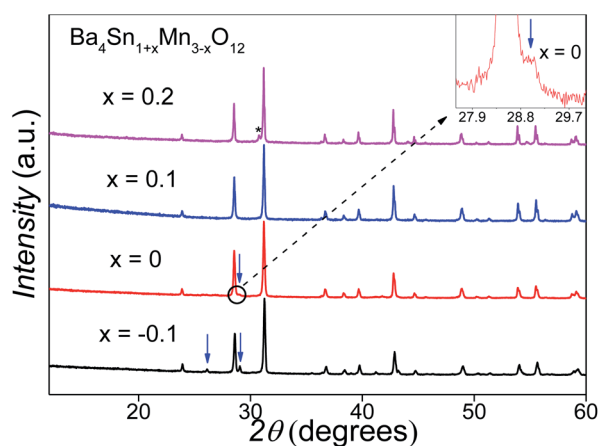


Fig. 2 X-ray diffraction patterns of our  $\text{Ba}_4\text{Sn}_{1+x}\text{Mn}_{3-x}\text{O}_{12}$  samples, showing a pure phase 12R perovskite at the  $x = 0.1$  composition. The inset enlarges the XRD plots of the  $x = 0$  sample for clarity. The reflections from 10H  $\text{Ba}_5\text{Sn}_{1.1}\text{Mn}_{3.9}\text{O}_{15}$  and  $\text{BaSnO}_3$  are marked with arrows and asterisks respectively.

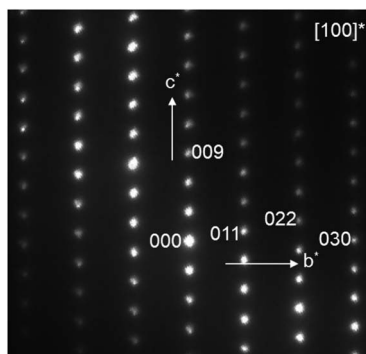


Fig. 3 The SAED patterns collected along [100] direction for  $\text{Ba}_4\text{Sn}_{1.1}\text{Mn}_{2.9}\text{O}_{12}$ . The indexations were performed using the hexagonal cell ( $a \sim 5.72 \text{ \AA}$  and  $c \sim 28.2 \text{ \AA}$ ).

a single-phase 12R product is obtained at the composition of  $\text{Ba}_4\text{Sn}_{1.1}\text{Mn}_{2.9}\text{O}_{12}$ . Further increasing the Sn substitution rate leads to a secondary Sn-rich cubic perovskite phase, *i.e.*  $\text{BaSnO}_3$ , as marked with an asterisk. The ICP analysis on the  $\text{Ba}_4\text{Sn}_{1.1}\text{Mn}_{2.9}\text{O}_{12}$  sample shows the Ba : Sn : Mn ratio of 4.03 : 1.07 : 2.84, which is essentially identical to the initial cationic ratio. This observation confirms the chemical composition of  $\text{Ba}_4\text{Sn}_{1.1}\text{Mn}_{2.9}\text{O}_{12}$  for the 12R perovskite phase.

The XRD pattern of  $\text{Ba}_4\text{Sn}_{1.1}\text{Mn}_{2.9}\text{O}_{12}$  is similar to that of  $\text{Ba}_4\text{NbMn}_3\text{O}_{12}$  (ref. 27) and can be indexed using a rhombohedral hexagonal unit cell with lattice parameters  $a = 5.7289(4) \text{ \AA}$ , and  $c = 28.163(3) \text{ \AA}$ . The selected area electron diffraction (SAED) pattern along [100] zone axis is shown in Fig. 3. No superstructure reflections are seen, and all the observed reflections agree with the indexing results. The systematic absence of the reflections  $h\bar{h}0l$ :  $h - l \neq 3n$  and  $000l$ :  $l \neq 3n$  is consistent with the space group  $R\bar{3}m$ .

### 3.2 Crystal structure

Due to their weak X-ray scattering ability, the light oxygen atoms are not well located with X-ray diffraction in the presence of heavy elements such as barium. Neutron diffraction (ND) is more sensitive to oxygen because the neutron scattering length of oxygen (5.083 fm) is comparable to that of Ba (5.07 fm).<sup>36</sup> Therefore, to find the oxygen position and possible vacancies, neutron diffraction data were collected on the  $\text{Ba}_4\text{Sn}_{1.1}\text{Mn}_{2.9}\text{O}_{12}$  sample. The Rietveld refinements against the XRD and ND data simultaneously were performed, using the 12R  $\text{Ba}_4\text{NbMn}_3\text{O}_{12}$  structural model (Fig. 1a). In the first step, the occupancies of Sn and Mn at M1, M2, and M3 sites were refined with the total occupancies on each site subject to unity. A negative value of Sn on the M3 site was found, excluding the presence of Sn at the M3 site. In the following refinement, the occupancies of Sn and

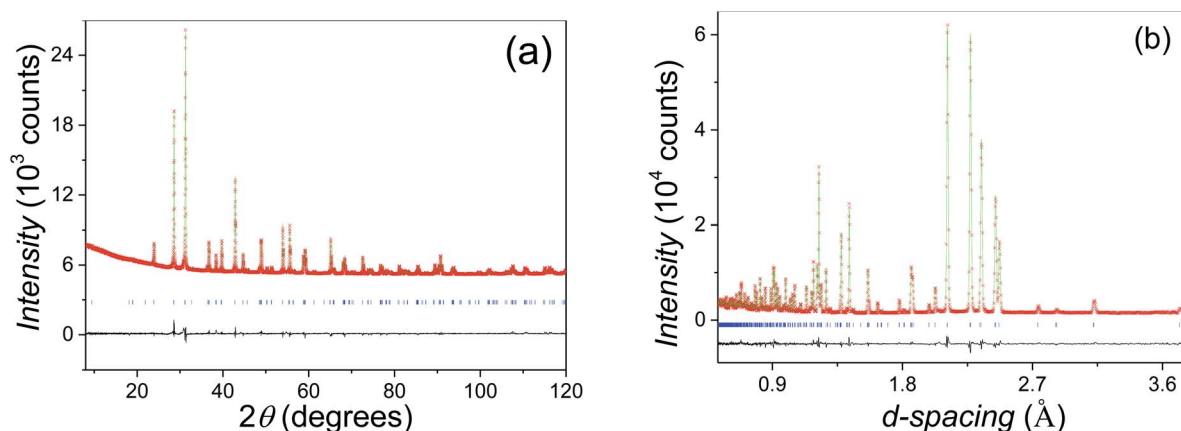


Fig. 4 Rietveld refinement plots of (a) XRD data and (b) ND data for the  $\text{Ba}_4\text{Sn}_{1.1}\text{Mn}_{2.9}\text{O}_{12}$  sample, showing observed (red crosses), calculated (green line) and difference curve (grey line). The blue bars mark the reflection positions for  $\text{Ba}_4\text{Sn}_{1.1}\text{Mn}_{2.9}\text{O}_{12}$  in both plots.

Table 1 Refined structural parameters of  $\text{Ba}_4\text{Sn}_{1.1}\text{Mn}_{2.9}\text{O}_{12}$ <sup>a</sup>

Atom	Site	$x, y, z$	Occupancy	Beq	BVS
Ba1	6c	2/3, 1/3, 0.04672(5)	1	0.94(7)	2.37
Ba2	6c	0, 0, 0.12840(4)	1	0.88(7)	2.23
(Sn/Mn) <sub>M1</sub>	3a	0, 0, 0	0.881(3)/0.119(3)	0.83(3)	4.24/2.81
(Mn/Sn) <sub>M2</sub>	6c	1/3, 2/3, 0.07695(8)	0.891(1)/0.109(1)	1.46(5)	3.84/5.43
Mn <sub>M3</sub>	3b	1/3, 2/3, 1/6	1	1.19(6)	4.10
O1	18h	0.48062(9), 0.51938(9), 0.12380(4)	1	1.07(6)	
O2	18h	0.49856(11), 0.50144(11), 0.29189(4)	1	1.20(6)	

<sup>a</sup>  $a = 5.72904(3) \text{ \AA}$ , and  $c = 28.1637(3) \text{ \AA}$  space group:  $R\bar{3}m$ .

Table 2 Selected bond lengths and angles of Ba<sub>4</sub>Sn<sub>1.1</sub>Mn<sub>2.9</sub>O<sub>12</sub>

Bond length (Å)	Bond length (Å)	Bond angle (degree)
(Sn/Mn) <sub>M1</sub> -O2 (×6) 2.0334 (10)	Mn <sub>M3</sub> -O1 (×6) 1.8933 (9)	(Sn/Mn) <sub>M1</sub> -O2-Mn <sub>M2</sub> 176.400 (2)
(Mn/Sn) <sub>M2</sub> -O1 (×3) 1.966 (3)	Mn <sub>M2</sub> -Mn <sub>M3</sub> 2.523 (5)	Mn <sub>M2</sub> -O1-Mn <sub>M3</sub> 81.626(3)
(Mn/Sn) <sub>M2</sub> -O2 (×3) 1.918 (3)		

Mn were refined only at M1 and M2 sites, with the ratio of Sn : Mn constrained by the initial stoichiometry. In the second step, the oxygen occupancies were refined, and no vacancies were found at both O1 and O2 sites within the refinement error. Therefore, the oxygen occupancies at both sites were set as unity. The final refinement gave a good fit (Fig. 4a and b), with overall  $R_{wp}$  and  $\chi^2$  parameters of 4.99% and 1.20 respectively. The refined structural parameters and selected bond distances and angles are listed in Tables 1 and 2, respectively. The Bq parameters for atoms of the same type on the different sites show a small difference within 20%. The large discrepancy of Bq parameters between the M1 and M2 sites keeps with their different dominated elements, *i.e.* Sn and Mn respectively.

In the crystal structure of 12R Ba<sub>4</sub>Sn<sub>1.1</sub>Mn<sub>2.9</sub>O<sub>12</sub>, the M1 site is dominated by the Sn atom (occupancy ~ 88.1%), and the M2 site is dominated by the Mn atom (occupancy ~ 89.1%). The BVS values of Mn atom at M1 and M2 sites (2.81 and 3.84 respectively) are smaller than 4, whilst that of Sn atom shows larger values than 4 (4.24 at M1 site and 5.43 at M2 site). This discrepancy arises from the mixed Sn and Mn occupancy because the average bond lengths are used in BVS calculations. But both Mn and Sn atoms most likely show the oxidation states of +4 on local M1 and M2 sites, although trace amounts of Mn<sup>3+</sup> at M1 site and compensating oxygen vacancies (within the refinement errors) cannot be excluded. Similar phenomena have been observed in the 10H Ba<sub>5</sub>Sn<sub>1.1</sub>Mn<sub>3.9</sub>O<sub>15</sub> polymorphs.<sup>18</sup>

It should be noted about the distortion of outer MnO<sub>6</sub> octahedra in the trimers. The Mn at the M2 site shifts toward the *c*-BaO<sub>3</sub> layers, forming three shorter Mn<sub>M2</sub>-O2 bonds (~1.91 Å) and three longer Mn<sub>M2</sub>-O1 bonds (~1.96 Å). The inner

Mn<sub>M3</sub>O<sub>6</sub> octahedron is undistorted and constrained by its local symmetry of  $D_{3d}$  on the M3 site. Due to the distortion, the Mn-Mn distance inside the trimers (~2.52 Å) is larger than that (2.407 Å) between undistorted MnO<sub>6</sub> octahedrons in 2H BaMnO<sub>3</sub>.<sup>37</sup> This suggests that octahedron distortion may help to stabilize the formation of MnO<sub>6</sub> octahedral trimers. This short Mn-Mn distance is comparable with that in elemental  $\alpha$ -Mn<sup>38</sup> and may suggest a degree of d-orbital overlap between neighboring Mn ions within each trimer forming Mn<sub>3</sub> (and minor Mn<sub>2</sub>) magnetic clusters.

Thermal stability was investigated by the temperature varied XRD, as shown in Fig. 5a. No phase transition exists in the title compound until 873 K. The lattice parameters increase linearly as the temperature increases, showing anisotropic thermal expansions of  $\alpha_a = 12.5 \times 10^{-6} \text{ K}^{-1}$  and  $\alpha_c = 10.6 \times 10^{-6} \text{ K}^{-1}$ . This leads to an overall linear volume expansion of  $\alpha_V = 35.9 \times 10^{-6} \text{ K}^{-1}$  at 300–873 K temperature range (Fig. 5b).

### 3.3 Magnetic properties

The temperature-dependent DC magnetic susceptibilities per Mn ions are shown in Fig. 6a. The susceptibilities change little at 150–300 K and start to increase steeply as the temperature goes down. The maximum value of ZFC susceptibility is observed at about 6.0 K, below which ZFC and FC data are divergent. It suggests an antiferromagnetic (AFM) phase transition around  $T_N = 6 \text{ K}$ .

Surprisingly, the magnetic susceptibilities above 6 K do not obey the Curie-Weiss law, as shown in Fig. 6b. The attempt fit on 150–300 K yields an  $\mu_{\text{eff}} = 4.2(1) \mu_B$  per Mn<sup>4+</sup>, reasonably close to the spin-only value of Mn<sup>4+</sup> 3.9  $\mu_B$ , but an enormously

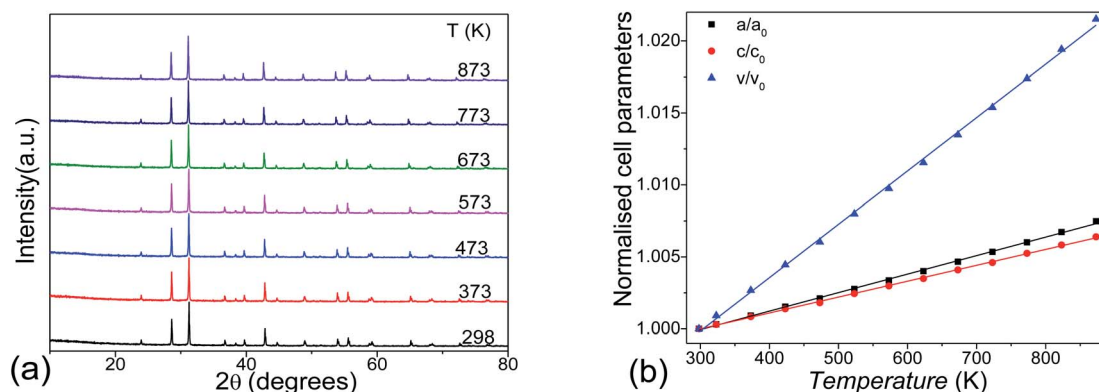
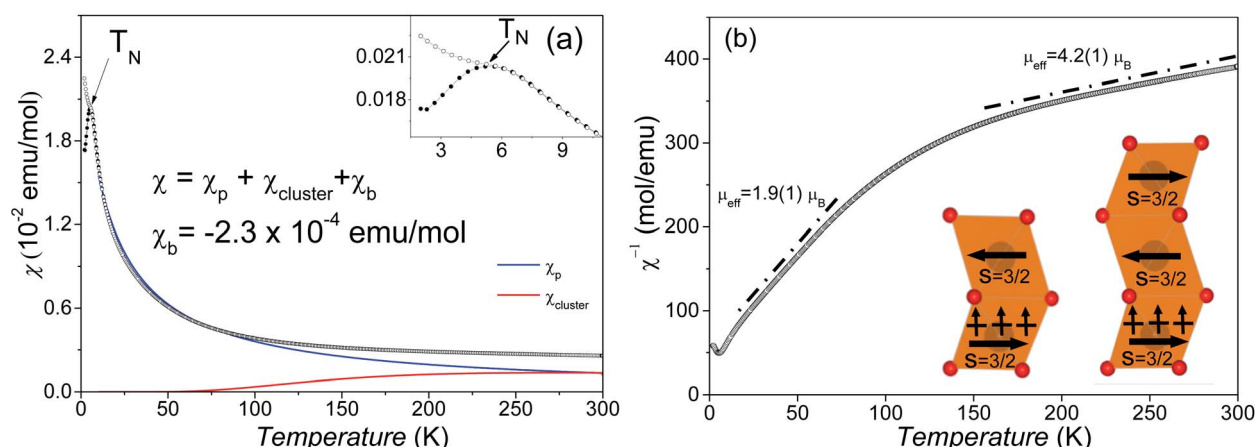


Fig. 5 Temperature-dependent (a) XRD data for Ba<sub>4</sub>Sn<sub>1.1</sub>Mn<sub>2.9</sub>O<sub>12</sub> and (b) cell parameters in relative to the RT values obtained from the XRD data ( $a_0 = 5.72904(3) \text{ Å}$ ,  $c_0 = 28.1637(2) \text{ Å}$ ,  $V_0 = 800.54(1) \text{ Å}^3$ ), with the fits shown as the solid lines.



**Fig. 6** (a) Temperature-dependent ZFC (filled circles) and FC (empty circles) magnetic susceptibilities for  $\text{Ba}_4\text{Sn}_{1.1}\text{Mn}_{2.9}\text{O}_{12}$  per mole of  $\text{Mn}(\text{IV})$ , with low-temperature data shown in the inset. The blue and red lines represent the fitted paramagnetic and the cluster contributions, noted as  $\chi_p$  and  $\chi_{\text{cluster}}$  respectively. (b) Inverse susceptibility per mole of  $\text{Mn}(\text{IV})$ . The dashed lines show the slopes corresponding to  $\mu_{\text{eff}} = 1.9 \mu_B$  and  $\mu_{\text{eff}} = 4.2(1) \mu_B$ . The inset to (b) shows the schematics of the possible simple hypothetical arrangements for  $\text{Mn}^{4+}$  ( $S = 3/2$ ) in the  $\text{Mn}_3$  and  $\text{Mn}_2$  magnetic clusters of  $\text{Ba}_4\text{Sn}_{1.1}\text{Mn}_{2.9}\text{O}_{12}$ .

large  $\theta_{\text{CW}} = -565$  K compared with  $T_N$ . The Curie–Weiss fit on 25–80 K yields a much smaller  $\mu_{\text{eff}} = 1.9(1) \mu_B$  per  $\text{Mn}^{4+}$  and a small  $\theta_{\text{CW}} = -22$  K. This reduced magnetic moment at intermediate temperatures indicates the formation of AFM magnetic clusters. Considering the crystal structure, the magnetic clusters are predominantly the  $\text{Mn}_3$  (Fig. 6b inset) inside the trimers of face-sharing  $\text{MnO}_6$  octahedra. The minor  $\text{Mn}_2$  clusters (Fig. 6b inset) are also present due to diamagnetic  $\text{Sn}^{4+}$  replacing  $\sim 10.9\%$   $\text{Mn}^{4+}$  on the M2 site. The  $\text{Mn}_3$  (and  $\text{Mn}_2$ ) magnetic linear clusters are observed in the 12R  $\text{Ba}_4\text{NbMn}_3\text{O}_{12}$  (ref. 27 and 30) and  $\text{Ba}_4\text{Ti}_2\text{Mn}_2\text{O}_{12}$  (ref. 31) perovskite. The susceptibility of these magnetic clusters,  $\chi_{\text{cluster}}$ , can be estimated using an analog expression of a spin  $S = \frac{1}{2}$  dimer.<sup>39</sup>

$$\chi_{\text{cluster}} = \frac{D}{T \times (1 + 1/3 \exp(2\theta'/T))}$$

$D$  is related to magnetic moments involved in cluster formation, while  $\theta'$  corresponds to the temperature cluster forms. The total

experimental susceptibilities  $\chi$  can be divided into three parts:  $\chi_{\text{cluster}}$ , a paramagnetic contribution  $\chi_p = C/(T - \theta)$ , and the constant term  $\chi_b$ . The last term  $\chi_b$  has two origins: the susceptibility of the sample capsule determined as  $-6.2 \times 10^{-6}$  emu (or equally  $-1.3 \times 10^{-4}$  emu mol $^{-1}$   $\text{Mn}^{4+}$ ) with a blank measurement, and the diamagnetic susceptibility of  $\text{Ba}_4\text{Sn}_{1.1}\text{Mn}_{2.9}\text{O}_{12}$ , which can be estimated to be  $-2.91 \times 10^{-4}$  emu f.u. $^{-1}$  (or equally  $-1.00 \times 10^{-4}$  emu mol $^{-1}$   $\text{Mn}^{4+}$ ) using Pascal's constant.<sup>40</sup> Therefore the constant term  $\chi_b$  is fixed as  $-2.3 \times 10^{-4}$  emu mol $^{-1}$   $\text{Mn}^{4+}$  in the following least-square fits against the 10–300 K susceptibilities.

Good fits were obtained (Fig. 6a), leading to  $C = 0.42(1)$  K emu Oe $^{-1}$ ,  $\theta = -17.1(1)$  K,  $D = 0.99(1)$  K emu Oe $^{-1}$ , and  $\theta' = 218.7(1)$  K. The negative Weiss constant indicates antiferromagnetic interactions between the Mn spins. The  $\theta = -17.1(1)$  K is comparable with the  $T_N$  as expected. The cluster formation temperature  $\theta'$  depends on the magnetic exchange interaction inside the  $\text{MnO}_6$  trimers and is reasonably close to the exchange

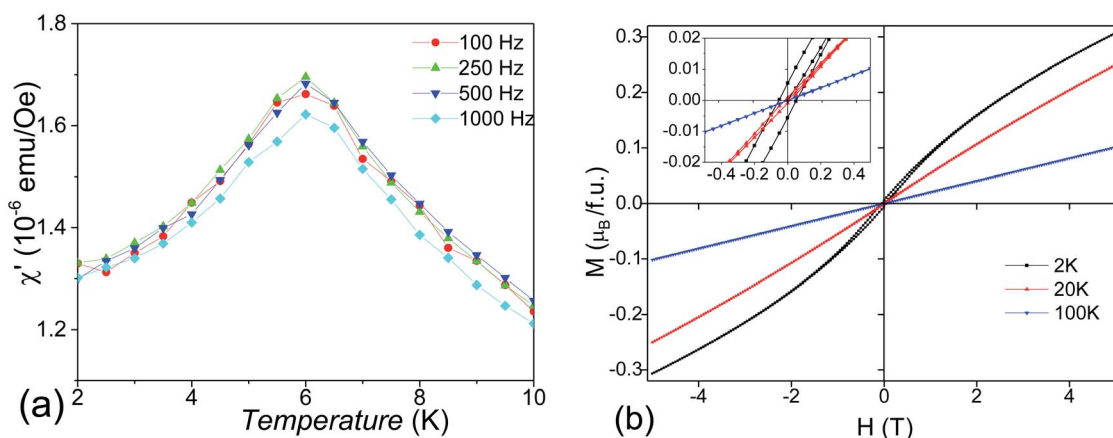


**Fig. 7** (a) Temperature-dependent AC magnetic susceptibilities  $\chi'$  at frequencies of 100–1000 Hz, (b) Isothermal  $M$ – $H$  curves at 2, 20, and 100 K for  $\text{Ba}_4\text{Sn}_{1.1}\text{Mn}_{2.9}\text{O}_{12}$  sample under the applied field of  $-5$  T to  $5$  T. The inset to (b) expands the  $M$ – $H$  curves at low field region.

constant ( $J_a/k_B = 200$  K) in the dimer and trimer of  $\text{MnO}_6$  octahedra.<sup>30</sup> The overall magnetic moment  $3.05(1) \mu_B \text{ mol}^{-1} \text{ Mn}^{4+}$ , as calculated using  $\mu_{\text{eff}} = (8C + 6D)^{1/2}$ , is lower than its spin-only value ( $3.87 \mu_B$ ). This small difference can be acceptable given the presence of both  $\text{Mn}_2$  and  $\text{Mn}_3$  clusters and the roughness of the cluster model. If we ignore the contribution of minor  $\text{Mn}_2$  clusters, then the effective magnetic moments  $\mu_{\text{eff}}$  per  $\text{Mn}_3$  linear cluster  $3.17(1) \mu_B$ , as calculated from  $(24C)^{1/2}$ , is essentially identical with the calculated value of  $3.05 \mu_B \text{ mol}^{-1} \text{ Mn}^{4+}$ . This observation seems coincidental and comes from the AFM nature of the  $\text{Mn}_3$  linear clusters. Similarly, the  $\text{Ba}_4\text{-NbMn}_3\text{O}_{12}$  has one  $\text{Mn}^{3+}$  ion and two  $\text{Mn}^{4+}$  ions in each trimer of  $\text{MnO}_6$  octahedra, thus the  $\mu_{\text{eff}}$  per  $\text{Mn}_3$  cluster is equal to the  $\mu_{\text{eff}}$  of  $\text{Mn}^{3+}$ .<sup>27,30</sup> The minor  $\text{Mn}_2$  clusters are expected to have a ground state of  $\mu_{\text{eff}} = 0 \mu_B$ . The residual Mn spins of dominant  $\text{Mn}_3$  clusters order at temperatures below  $T_N = 6$  K *via* antiferromagnetic  $\text{Mn}^{4+}\text{-O-(Sn}^{4+}/\text{Mn}^{4+})_{\text{M1}}\text{-O-Mn}^{4+}$  exchange interactions. Similar AFM order below 10 K has been observed for the 12R  $\text{Ba}_4\text{MMn}_3\text{O}_{12-\delta}$  ( $M = \text{Y, Nb, and Ce}$ ) with  $\text{Mn}_3$  linear clusters.<sup>25-27</sup>

In addition, the AC magnetic susceptibility  $\chi'$  shows a frequency-independent maximum at about 6 K, as shown in Fig. 7a. This observation rules out a spin glass transition at  $T_N = 6$  K and suggests the long-range AFM transition instead. The AFM order is most likely canted, which leads to a weak

ferromagnetic component below  $T_N$ , although further neutron diffraction study would be useful to characterize this ground state more fully. This is evidenced by small magnetic hysteresis and saturation in the 2 K  $M$ - $H$  curve (Fig. 7b), showing magnetic anisotropy with coercive fields of 50 mT and a saturated moment  $M_s = 0.09(1) \mu_B$ . These ferromagnetic components disappear above  $T_N$ , as indicated by the linear  $M$ - $H$  curve at 20 K and 100 K. The weak ferromagnetism below  $T_N$  may come from trace amounts of  $\text{Mn}^{3+}$  at M1 site. The hexagonal average lattice symmetry does not allow long-range orbital order, but when  $\text{Mn}^{3+}$  ions are present at the M1 sites, local orbital order with respect to the  $\text{Mn}^{4+}$  ions at the six neighboring M2 sites is likely in such a highly connected manganite network. This gives rise to ferromagnetic  $\text{Mn}_{\text{M1}}\text{-O-Mn}_{\text{M2}}$  interactions, as found in long-range orbitally ordered  $\text{La}_{0.5}\text{Ca}_{0.5}\text{MnO}_3$ .<sup>41</sup>

### 3.4 Conductivity and morphology

To explore the transport properties of  $\text{Ba}_4\text{Sn}_{1.1}\text{Mn}_{2.9}\text{O}_{12}$ , AC impedance data was collected on the dense pellet, which has 93% of the theoretical density. Fig. 8a shows typical complex impedance plots at 573 K measured at different atmospheres, which are essentially identical and consist of one asymmetric semicircle arc. The capacitances for this arc vary within  $10^{-12}$  to  $10^{-11} \text{ F cm}^{-1}$ , which could be ascribed to mixed bulk and grain boundary responses. No apparent electrode responses were observed in the impedance data. Fig. 8b shows the total conductivities of the  $\text{Ba}_4\text{Sn}_{1.1}\text{Mn}_{2.9}\text{O}_{12}$  pellets, which are almost independent of atmospheres. This keeps with very low content of oxygen vacancies in  $\text{Ba}_4\text{Sn}_{1.1}\text{Mn}_{2.9}\text{O}_{12}$ . The conductivities vary from  $10^{-11}$  to  $10^{-6} \text{ S cm}^{-1}$  in the temperature range 473–750 K. The Arrhenius plots show constant activation energy ( $E_a$ ) of  $0.61(1) \text{ eV}$  for the  $\text{Ba}_4\text{Sn}_{1.1}\text{Mn}_{2.9}\text{O}_{12}$ .

The SEM images in backscattering mode (Fig. 9) show the cross-section morphology of  $\text{Ba}_4\text{Sn}_{1.1}\text{Mn}_{2.9}\text{O}_{12}$  ceramic, which has homogeneous elements distribution and well-defined grain boundaries. The grain sizes are mainly distributed in the range

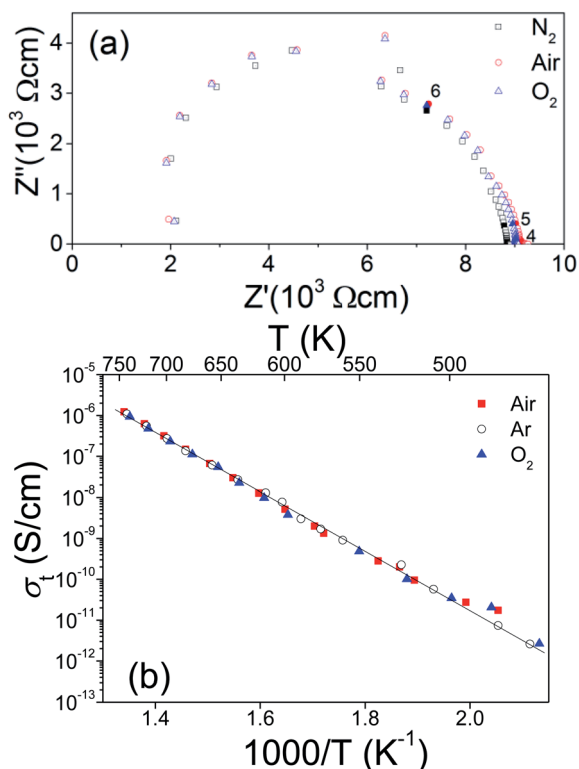


Fig. 8 (a) The 573 K complex impedance plots for  $\text{Ba}_4\text{Sn}_{1.1}\text{Mn}_{2.9}\text{O}_{12}$  pellets measured at the air, argon, and oxygen atmosphere. The numbers denote the logarithms of selected frequencies marked by filled symbols. (b) Temperature-dependent total conductivity of  $\text{Ba}_4\text{-Sn}_{1.1}\text{Mn}_{2.9}\text{O}_{12}$  pellets in air, oxygen and argon, showing constant activation energy of  $0.61(1) \text{ eV}$  regardless of the atmosphere.

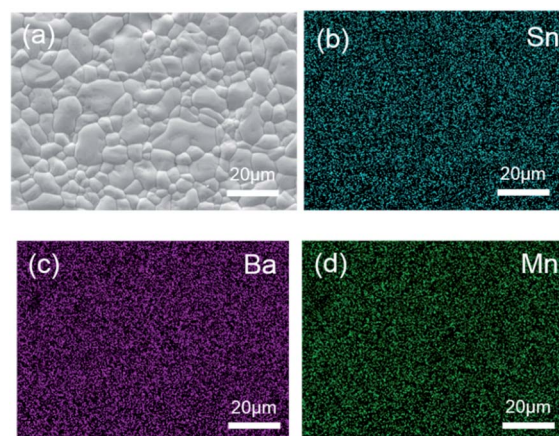


Fig. 9 Microstructure of the  $\text{Ba}_4\text{Sn}_{1.1}\text{Mn}_{2.9}\text{O}_{12}$  ceramic. (a) SEM image in backscattering mode showing homogeneous elements distribution and well-defined grain boundaries, and EDS mapping images of (b) Ba, (c) Sn, and (d) Mn.

of 2–10  $\mu\text{m}$  range (Fig. 9a), without significantly anisotropic grain growth, keeping with its good density. The Ba, Sn, Mn elements are uniformly distributed in the cross-section of the pellet, and the Ba : Sn : Mn ratio of 3.8 : 1.1 : 2.5 keeps with their stoichiometric ratio (Fig. 9b–d).

## 4 Conclusions

The new 12R perovskite  $\text{Ba}_4\text{Sn}_{1.1}\text{Mn}_{2.9}\text{O}_{12}$  has been synthesized by high-temperature solid-state reactions. The material has an ordered arrangement of Sn and Mn cations, and trimers of face-sharing  $\text{MnO}_6$  octahedra arranged in triangular plains. Within trimers of  $\text{MnO}_6$  octahedra, the outer  $\text{MnM}_2\text{O}_6$  octahedra are distorted but the inner  $\text{MnM}_3\text{O}_6$  octahedra are undistorted. The magnetism of  $\text{Ba}_4\text{Sn}_{1.1}\text{Mn}_{2.9}\text{O}_{12}$  perovskite can be described in the picture of molecular-like  $\text{Mn}_3$  and minor  $\text{Mn}_2$  linear clusters. These magnetic cluster forms at  $\sim 220$  K due to the strong AFM interaction inside the clusters, and has the effective moment of one  $\text{Mn}^{4+}$  spin per  $\text{Mn}_3$  cluster and zero spin per  $\text{Mn}_2$  cluster. Weaker inter-cluster magnetic interaction ordered these magnetic clusters antiferromagnetically at lower temperature  $T_N \sim 6$  K. The  $\text{Ba}_4\text{Sn}_{1.1}\text{Mn}_{2.9}\text{O}_{12}$  sample has a semi-conducting behavior with a transport activation energy of 0.61 eV.  $\text{Ba}_4\text{Sn}_{1.1}\text{Mn}_{2.9}\text{O}_{12}$  is another rare example of a periodical lattice that shows molecular-like cluster magnetism due to the cationic order beyond orbital molecules.<sup>42</sup>

## Conflicts of interest

There are no conflicts to declare.

## Acknowledgements

The National Natural Science Foundation of China (No. 51662013, 22161014, 21850410458), Guangxi Natural Science Foundation (No. 2020GXNSFAA297220, 2019GXNSFGA245006, AD19245097), and the Foundation of Guilin University of Technology (No. GUTQDJJ2018115) are acknowledged for their financial support. We acknowledge Prof. He Lunhua at China Spallat Neutron Source for the support in neutron data collection in this work.

## Notes and references

- 1 Q. Feng, H. Kanoh and K. Ooi, *J. Mater. Chem.*, 1999, **9**, 319–333.
- 2 P. Strobel and C. Mouget, *Mater. Res. Bull.*, 1993, **28**, 93–100.
- 3 A. R. Armstrong and P. G. Bruce, *Nature*, 1996, **381**, 499–500.
- 4 M. Mogensen, K. V. Jensen, M. J. Jørgensen and S. Primdahl, *Solid State Ionics*, 2002, **150**, 123–129.
- 5 G. H. Jonker and J. H. Van Santen, *Physica*, 1950, **16**, 337–349.
- 6 J. M. Longo and J. A. Kafalas, *J. Solid State Chem.*, 1969, **1**, 103–108.
- 7 T. Negas and R. S. Roth, *J. Solid State Chem.*, 1971, **3**, 323–339.
- 8 J. M. Gonzalez-Calbet, M. Parras, J. M. Alonso and M. Valletregi, *J. Solid State Chem.*, 1993, **106**, 99–110.
- 9 J. J. Adkin and M. A. Hayward, *J. Solid State Chem.*, 2006, **179**, 70–76.
- 10 J. J. Adkin and M. A. Hayward, *Chem. Mater.*, 2007, **19**, 755–762.
- 11 J. Varignon and P. Ghosez, *Phys. Rev. B: Condens. Matter Mater. Phys.*, 2013, **87**, 140403.
- 12 N. Floros, C. Michel, M. Hervieu and B. Raveau, *Chem. Mater.*, 2000, **12**, 3197–3201.
- 13 N. Floros, C. Michel, M. Hervieu and B. Raveau, *J. Solid State Chem.*, 2002, **168**, 11–17.
- 14 G. M. Keith, C. A. Kirk, K. Sarma, N. M. Alford, E. J. Cussen, M. J. Rosseinsky and D. C. Sinclair, *Chem. Mater.*, 2004, **16**, 2007–2015.
- 15 L. Miranda, A. Feteira, D. Sinclair, K. Boulahya, M. Hernando, J. Ramirez, A. Varela, J. M. Gonzalez-Calbet and M. Parras, *Chem. Mater.*, 2009, **21**, 1731–1742.
- 16 N. Créon, C. Michel, M. Hervieu, A. Maignan and B. Raveau, *Solid State Sci.*, 2003, **5**, 243–248.
- 17 C. L. Yin, G. B. Li, T. N. Jin, L. P. You, J. L. Tao, J. W. Richardson, C. Loong, J. L. Sun, F. H. Liao and J. H. Lin, *Chem. Mater.*, 2008, **20**, 2110–2116.
- 18 C. L. Yin, G. B. Li, T. N. Jin, J. L. Tao, J. W. Richardson, C. Loong, F. H. Liao and J. H. Lin, *J. Alloys Compd.*, 2010, **489**, 152–156.
- 19 C. L. Yin, G. B. Li, W. A. Kockelmann, F. H. Liao, J. P. Attfield and J. H. Lin, *Chem. Mater.*, 2010, **22**, 3269–3276.
- 20 L. Miranda, D. C. Sinclair, M. Hernando, A. Varela, A. Wattiaux, K. Boulahya, J. M. Gonzalez-Calbet and M. Parras, *Chem. Mater.*, 2009, **21**, 5272–5283.
- 21 J. G. Zhao, L. X. Yang, Y. Yu, F. Y. Li, R. C. Yu and C. Q. Jin, *J. Solid State Chem.*, 2008, **181**, 1767–1775.
- 22 C. L. Yin, G. B. Li, W. A. Kockelmann, J. H. Lin and J. P. Attfield, *Phys. Rev. B: Condens. Matter Mater. Phys.*, 2009, **80**, 094420.
- 23 N. A. Jordan and P. D. Battle, *J. Mater. Chem.*, 2003, **13**, 2220–2226.
- 24 A. F. Fuentes, K. Boulahya and U. Amador, *J. Solid State Chem.*, 2004, **177**, 714–720.
- 25 M. A. Macías, O. Mentre, S. Colis, G. J. Cuello and G. H. Gauthier, *J. Solid State Chem.*, 2013, **198**, 186–191.
- 26 X. J. Kuang, C. Bridges, M. Allix, J. B. Claridge, H. Hughes and M. J. Rosseinsky, *Chem. Mater.*, 2006, **18**, 5130–5136.
- 27 L. T. Nguyen, T. Kong and R. J. Cava, *Mater. Res. Express*, 2019, **6**, 056108.
- 28 R. D. Shannon, *Acta Crystallographica Section A*, 1976, **32**, 751–767.
- 29 M. A. Macías, O. Mentre, C. Pirovano, P. Roussel, S. Colis and G. H. Gauthier, *New J. Chem.*, 2015, **39**, 829–835.
- 30 S. V. Streltsov and D. I. Khomskii, *JETP Lett.*, 2018, **108**, 686–690.
- 31 F. A. Garcia, U. F. Kaneko, E. Granado, J. Sichelschmidt, M. Hölzel, J. G. S. Duque, C. A. J. Nunes, R. P. Amaral, P. Marques-Ferreira and R. Lora-Serrano, *Phys. Rev. B: Condens. Matter Mater. Phys.*, 2015, **91**, 224416.
- 32 A. J. Browne, A. Krajewska and A. S. Gibbs, *J. Mater. Chem. C*, 2021, **9**, 11640–11654.

- 33 L. T. Nguyen and R. J. Cava, *Chem. Rev.*, 2021, **121**, 2935–2965.
- 34 A. Coelho, *Topas Academic Version 5*, Coelho Software, Brisbane, Australia, 2012.
- 35 I. D. Brown and D. Altermatt, *Acta Crystallogr., Sect. B: Struct. Sci.*, 1985, **41**, 244–247.
- 36 V. F. Sears, *Neutron News*, 1992, **3**, 26–37.
- 37 E. J. Cussen and P. D. Battle, *Chem. Mater.*, 2000, **12**, 831–838.
- 38 J. A. Oberteuffer and J. A. Ibers, *Acta Crystallogr., Sect. B: Struct. Sci.*, 1970, **26**, 1499–1504.
- 39 F. E. Mabbs and D. J. Machin, *Magnetism and Transition Metal Complexes*, Dover Publication, Inc., Mineola, New York, 2007.
- 40 G. A. Bain and J. F. Berry, *J. Chem. Educ.*, 2008, **85**, 532–536.
- 41 E. Dagotto, T. Hotta and A. Moreo, *Phys. Rep.*, 2001, **344**, 1–153.
- 42 J. P. Attfield, *APL Mater.*, 2015, **3**, 041510.